Intermolecular coupling and superconductivity in $PbMo_6S_8$ and other Chevrel phase compounds

Jia Chen,[1] Andrew J. Millis,[2,3] and David R. Reichman[1]
[1]*Department of Chemistry, Columbia University, New York, New York 10027, USA*
[2]*Department of Physics, Columbia University, New York, New York 10027, USA*
[3]*Center for Computational Quantum Physics, The Flatiron Institute, New York, New York 10010, USA*

(Received 18 September 2018; published 26 November 2018)

To understand superconductivity in Chevrel phase compounds and guide the search for interesting properties in materials created with Chevrel phase molecules as building blocks, we use *ab initio* methods to study the properties of single Mo_6X_8 molecules with $X = S$, Se, Te as well as the bulk solid $PbMo_6S_8$. In bulk $PbMo_6S_8$, the different energy scales from strong to weak are the band kinetic energy, the intramolecular Coulomb interaction, the on-molecule Jahn-Teller energy, and the Hund's exchange coupling. The metallic state is stable with respect to Mott and polaronic insulating states. The bulk compound is characterized by a strong electron-phonon interaction with the largest coupling involving phonon modes with energies in the range from 11 to 17 meV and with a strong intermolecule (Peierls) character. A two-band Eliashberg equation analysis shows that the superconductivity is strong coupling, with different gaps on the two Fermi surface sheets. A Bergman-Rainer analysis of the functional derivative of the transition temperature with respect to the electron-phonon coupling reveals that the Peierls modes provide the most important contribution to the superconductivity. This work illustrates the importance of intermolecular coupling for collective phenomena in molecular solids.

DOI: 10.1103/PhysRevMaterials.2.114801

I. INTRODUCTION

Synthetic chemists are now able to assemble molecular clusters into crystal structures with atomic precision [1], making the search for collective and emergent properties in those superatomic solids a timely and important topic. The notion of bootstrapping interesting molecular properties and strong molecular interactions into important bulk properties is an important theme in the field. For example, the relatively high transition temperature superconductivity in some members of the alkali-doped fullerenes is believed to arise from intramolecular vibrational modes [2,3] whereas in other alkali-doped fullerenes it is argued [4] to arise from intramolecular electron-electron interactions. The recent discovery of superconductivity in endohedral gallide clusters also exemplifies the rich set of possibilities provided by molecular solids [5].

Binary and ternary molybdenum chalcogenides, also known as Chevrel phase compounds [6], are of great interest in this context. Their chemical formula is $M_mMo_6X_8$, where M is a metal element and $X = S$, Se, Te. The bulk compound can be viewed as a molecular crystal of Mo_6X_8 units on the sites of a rhombohedral lattice, with the metal ions M in interstitial sites. The materials have been of sustained interest to both physicists and chemists because they can be superconducting with transition temperatures as high as 15 K ($PbMo_6S_8$) [7] and a high upper critical field [7–9]. Despite some hints at unconventional superconductivity [10,11], it is generally accepted that the electron-phonon interaction provides the pairing mechanism [12,13]. Chevrel compounds have also been proposed as promising multivalent cathode materials in Mg batteries [14]. Recent experimental efforts have been directed at synthesis of lower-dimensional Chevrel phase compounds [15].

Since Chevrel phase compounds are built of Mo_6X_8 molecular clusters, it is natural to approach the physics via a model of relatively weakly coupled clusters [16–18]. But, if this model is sufficient to understand superconductivity in Chevrel phase compounds is still not clear: specifically, the role of the intracluster and intercluster vibrational modes [19] in the superconductivity needs to be established.

In this paper, we analyze $PbMo_6S_8$ as a model system to gain insight into the role of intrasite and intersite interactions in molecular crystals and into the specifics of superconductivity in the Chevrel materials. To approach this system, we first calculate properties of isolated Mo_6X_8 molecules and use the results to derive and parametrize effective Hamiltonians including electron-electron and electron-phonon couplings. We study the bulk properties of $PbMo_6S_8$, calculating electron and phonon band structures, the electron-phonon coupling, and the intramolecular Coulomb interaction. Migdal-Eliashberg theory is then used to calculate the phonon renormalization of the bands and the superconducting gap functions and transition temperatures. Our key result is that the picture of intramolecular interactions combined with weak constant electronic hopping between molecular units is not an adequate description of the bulk compounds. Intermolecule effects, most notably phonons that simply do not exist in the single-molecule case except as a translation or a rotation of model, play a crucial role in setting the electronic properties including superconductivity while the intramolecular couplings have significantly weaker effects. Screening of the intramolecular Coulomb interaction is of significant importance in Chevrel phase compounds.

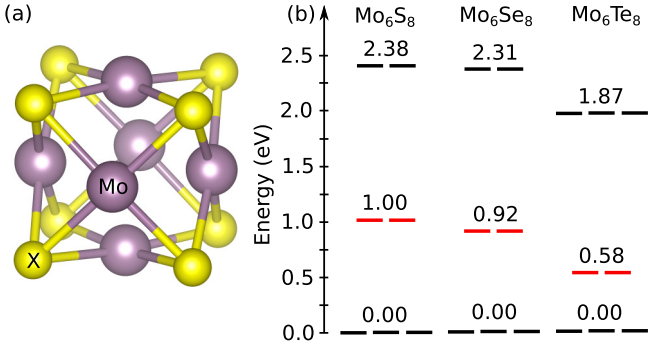

FIG. 1. (a) Structure of Mo_6X_8 molecule; (b) relative HOMO, first and second LUMO levels of neutral Mo_6S_8, Mo_6Se_8, and Mo_6Te_8. The HOMO levels of all three are set to 0.

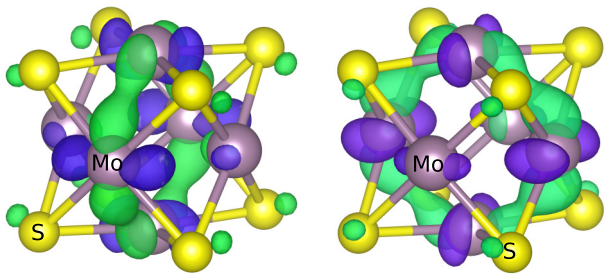

FIG. 2. Twofold-degenerate LUMO orbitals of neutral Mo_6S_8 generated by VESTA3 [25]. The value for isosurface in the plot was chosen to be 0.02 a.u.

This paper is organized as follows. In Sec. II, we consider isolated Mo_6X_8 molecules, identifying the important low-energy degrees of freedom and interactions within the building blocks of the solids. Sections III and IV discuss electron and phonon band structures, Hubbard U, Hund's exchange J, and electron-phonon interaction in bulk $PbMo_6S_8$. In Sec. V, we present the consequences of the electron-phonon interaction and diagnose which phonons are most important for superconductivity. Section VI is a conclusion.

II. MOLECULAR PROPERTIES

Molecular solids such as the Chevrel phase materials are composed of molecular building blocks (Mo_6X_8 in the present case) held together with other elements (metal ions such as Pb, in the present case). The first step in understanding the properties of molecular solids is to determine the relevant orbitals of the building blocks, and the electron-electron and electron-phonon interactions relevant to these orbitals. To obtain this information we study properties of isolated neutral and charged Mo_6X_8 molecules using density functional theory (DFT) methods with the PW91 generalized gradient approximation exchange-correlation functional [20] as implemented in the NWCHEM package [21]. The basis set for molybdenum, selenium, tellurium is LANL2DZ [22], and for sulfur is 6-31G** [23,24].

Neutral Mo_6X_8 molecules [shown Fig. 1(a)] have the symmetry of the O_h point group. Figure 1(b) shows that the highest occupied molecular orbitals (HOMO) are threefold degenerate while the lowest unoccupied molecular orbitals (LUMO) are twofold degenerate and transform according to the E_g representation of O_h. We focus on the LUMO doublet here because in the bulk solids of interest the M ions transfer electrons to the Mo_6X_8 clusters, so the Fermi level lies in bands derived from these orbitals. Energetically, the E_g orbitals are separated from other molecular orbitals by 1.0 eV in Mo_6S_8; this separation becomes smaller for Mo_6Se_8 and Mo_6Te_8. Plots of the E_g orbitals are shown in Fig. 2: each of those two orbitals approximately consists of $d_{x^2-y^2}$ orbitals arising from four coplanar Mo ions.

We can estimate the intramolecular electron-electron interaction U of isolated $Mo_6X_8^{2-}$ from the charging energy: $U = E_{Mo_6X_8^{3-}} + E_{Mo_6X_8^{1-}} - 2E_{Mo_6X_8^{2-}}$ and Hund's exchange J from the energy difference between singlet and triplet: $2J = E^{\text{singlet}}_{Mo_6X_8^{2-}} - E^{\text{triplet}}_{Mo_6X_8^{2-}}$. From Table II, we can see $U \approx 3.5$ eV for Mo_6X_8 molecules. $J \approx 100$ meV for all three molecules, and is just large enough to overcome the Jahn-Teller electron phonon coupling in $Mo_6X_8^{2-}$ molecules as discussed below.

We now turn to the electron-phonon coupling, focusing on those modes that couple linearly to the LUMO orbitals. Phonons couple to electron bilinearly; the electrons transform as the E_g representation of O_h and the direct product of two E_g representations of the O_h group can be reduced as $E_g \times E_g = a_{1g} + a_{2g} + e_g$, so we need to consider only vibrational modes belonging to the a_{1g}, a_{2g}, and e_g representations. The e_g mode is Jahn-Teller active, which means it can lift the degeneracy and lower the symmetry of the molecule. The phonon frequencies and normal mode vectors are computed by diagonalizing Hessian matrix, leading to a phonon plus electron-phonon Hamiltonian which we write representing the phonons in a first quantized form using a normalized phonon operator Q. For A-symmetry (scalar) phonons we have

$$\mathcal{H}(Q_\alpha) = \frac{\hbar\omega_\alpha}{2}\left(-\frac{\partial^2}{\partial Q_\alpha^2} + Q_\alpha^2\right) + g_\alpha Q_\alpha n_{el}, \tag{1}$$

where n_{el} is the number of electrons in the LUMO states, α labels phonon modes, and g_α is electron-vibration interaction. g_α is electron-vibration interaction matrix element

$$g_\alpha = \langle\psi|\frac{\partial V}{\partial Q_\alpha}|\psi\rangle, \tag{2}$$

where V is electron-ion interaction potential, and $|\psi\rangle$ is the LUMO orbital.

For e-symmetry (doublet) phonon modes we represent the mode as a two-component vector $\vec{Q} = (Q^x, Q^z)$ and write

$$\mathcal{H}(\vec{Q}_\alpha) = \frac{\hbar\omega_\alpha}{2}\left(-\frac{\partial^2}{\partial \vec{Q}_\alpha^2} + |\vec{Q}_\alpha|^2\right) + g_\alpha \vec{Q}_\alpha \cdot \sum_{ab\sigma} d^\dagger_{a\sigma}\vec{\tau}^{ab} d_{b\sigma}, \tag{3}$$

where τ is a Pauli matrix and a, b label the two states of the electronic E_g doublet.

The adiabatic potential energy surface (APE) for phonon mode α is defined as the ground-state eigenvalue of Eqs. (1) and (3) with the kinetic energy (∂_{Q_α}) terms neglected. The difference between the value at the minimum and the value at $Q = 0$ defines the phonon stabilization energy

$$\omega_{\text{eff},\alpha} = \frac{g_\alpha^2 \rho_{el}^2}{2\omega_\alpha}. \tag{4}$$

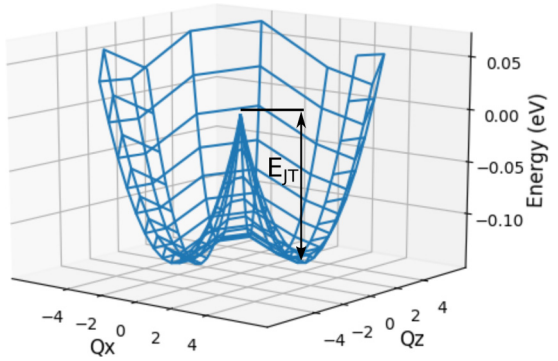

FIG. 3. Adiabatic potential energy surface of Mexican hat shape calculated for the e_g vibrational mode of $Mo_6S_8^{2-}$ at 31.0 meV with the occupation of two electrons ($n = 2$). Q_x and Q_z are degenerate vibrational modes, and they are renormalized by $\sqrt{\frac{\hbar}{m\omega}}$, thus dimensionless. E_{JT} is Jahn-Teller stability energy due to structural distortion.

Here, ρ_{el} is the LUMO occupancy for the A-symmetry modes and is the maximal orbital disproportionation ($\rho = 1$ for $n = 1, 3$ and $\rho = 2$ for $n = 2$) in the E (Jahn-Teller) case. The coupling constants g_α are determined from the calculated APEs.

For A-symmetry phonons the APE is a parabola with minimum at $Q_\alpha = -\frac{g_\alpha n_{el}}{\omega_\alpha}$. We find two A modes, with frequencies of 41.6 and 50.4 meV. The associated stabilization energies are 0.2 and 7 meV, respectively, too small to be of relevance to the issues discussed here. We neglect the A-symmetry phonons henceforth.

For the E (doublet) phonons, the APE has the familiar "mexican hat" form shown for one of the phonons in Fig. 3. At the quadratic level considered here, the theory has the full $O(2)$ symmetry in the phonon modes, so energy is a function only of $\rho = |\vec{Q}|$. Higher-order terms in Q lift the degeneracy leading to three degenerate minima (visible on close inspection in Fig. 3) as required by the O_h symmetry. We find two E-symmetry modes; their frequencies, linear coupling parameters, and stabilization energies as function of occupations of LUMO states are listed in Table I for Mo_6S_8. The coupling of the mode at high frequency is much larger than that of the mode at low frequency. As the occupation number increases, the vibrational modes become slightly softer and the linear coupling parameter g becomes weaker. The total stabilization energy is the sum of the stabilization

TABLE I. Quadratic frequency, linear coupling energy, and the Jahn-Teller stabilization energy for occupation number $n = 1, 2, 3$. For the neutral molecule, $\omega_1 = 32.8$ meV and $\omega_2 = 29.9$ meV. For occupation $n = 4$, the Jahn-Teller effect is no longer active, but mode softening is still visible.

Occupation modes	$n=1$ ω_1	$n=1$ ω_2	$n=2$ ω_1	$n=2$ ω_2	$n=3$ ω_1	$n=3$ ω_2
ω (meV)	31.8	28.4	31.0	27.8	28.5	27.3
g (meV)	49.4	27.0	46.0	23.8	38.8	18.8
$k = g/\omega$	1.55	0.95	1.48	0.86	1.36	0.69
E_{JT} (meV)	38.4	12.8	136.2	40.8	26.4	6.5

TABLE II. Total Jahn-Teller stabilization energy, charging energy, and Hund's exchange for $Mo_6X_8^{2-}$.

	$Mo_6S_8^{2-}$	$Mo_6Se_8^{2-}$	$Mo_6Te_8^{2-}$
E_{JT} (meV)	186	145	86
J (meV)	103	100	90
U (eV)	3.7	3.5	3.4

energies of the two modes and is shown in Table II for the three different choices of calcogen ions. As the chalcogenide elements become heavier, the Jahn-Teller stabilization energy decreases significantly, which correlates with the manner in which size and flexibility of the molecules change with chalcogenide element.

In the isolated singly charged molecule $Mo_6X_8^{1-}$, the Jahn-Teller effect ($E_{JT} \approx 50$ meV) is unopposed and we expect the molecule to distort away from a cubic shape. For the doubly charged $Mo_6X_8^{2-}$, the Jahn-Teller energy is about four times as large as it is for the singly charged case, however, the distortion energy is reduced by the Hund's exchange J ($\approx$100 meV). Our calculation indicates a spin-triplet ground state for $Mo_6X_8^{2-}$, but the energy difference is small enough that this conclusion should be treated as preliminary. The large value of the onsite Coulomb interaction, which is much greater than the $n = 2$ Jahn-Teller stability energy, implies that an ensemble of singly charged molecules will not disproportionate into bipolarons.

The Jahn-Teller stabilization energy is a useful measure for comparing the relative strengths of the Jahn-Teller effects across different material families. The stabilization energy 186 meV we find for Mo_6S_8 at $n = 2$ is smaller than the 500 meV found in $LaMnO_3$ [26] or the 215 and 341 meV found for $LiMnO_2$ and $LiCuO_2$ [27].

III. BULK COMPOUND: ELECTRONIC PROPERTIES

A. Electronic band structure

We next study the electronic structure of $PbMo_6S_8$ solid via DFT calculations with PBE as exchange-correlation functional [28], as implemented in the QUANTUM ESPRESSO package [29]. Unless otherwise noted, the structures are fully relaxed both in terms of atomic positions and lattice constants. Norm-conserving separable dual-space Gaussian pseudopotentials [30] were used for all elements. The kinetic energy cutoff for wave functions is 80 Rydberg and the convergence threshold for force is 1.0×10^{-4} Hartree/bohr. Structural relaxations are done with $4 \times 4 \times 4$ Brillouin zone grid; and band structure calculations are also done with density generated on that k-point grid.

The left panel of Fig. 4 shows the band structure and density of states (DOS) of $PbMo_6S_8$. The relaxed lattice constant and bond angle are $a = 6.55$ Å and $\alpha = 89.12^\circ$, in good agreement with experimental values of $a = 6.55$ Å and $\alpha = 89.33^\circ$ [31]. Consistent with the single-molecule results, we see that only two bands cross the Fermi level; these are derived from the E_g states discussed above. The bandwidth of the two E_g-derived bands is $W \approx 0.7$ eV. Near the R point the energy of the E_g bands is lower than that of the other filled bands, but there are no band crossings, thus no band

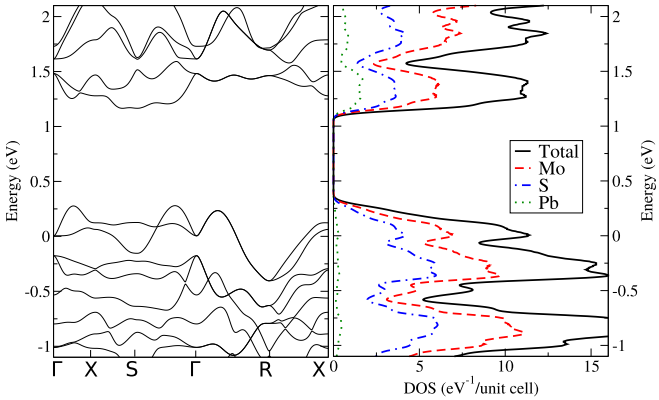

FIG. 4. Band structure (left panel) and density of states (right panel) of $PbMo_6S_8$. Since the unit cell is very close to be orthorhombic, we used high-symmetry points of simple orthorhombic lattice in band structure. The Fermi level is set to 0.

entanglement, enabling a straightforward Wannier analysis of the two conduction bands. The right panel shows the total density of states and its projection onto the component atoms. The dominant contribution to the density of states near Fermi surface is from Mo orbitals, with some contribution from S and negligible contribution from Pb. The Fermi level is at a local and sharply peaked maximum in the density of states, consistent with previous arguments by Andersen and co-workers [18] based on the pressure dependence of the superconducting transition temperature. The total DOS at Fermi level is $N_{BS} = 10.8/(\text{eV unit cell})$, about a factor of 4 smaller than the experimental value $N_\gamma = 44.4/(\text{eV unit cell})$. (See Ref. [32] and references therein.) The dominant source of the difference is the electron-phonon coupling, as we will show below.

Using the WANNIER90 [33] implementation of the maximally localized Wannier function method [34] we studied the two E_g bands around Fermi level in some detail. From our calculation, the total occupation of these two bands is 2.0, which is consistent with a scenario in which each Pb transfers two electrons to a Mo_6S_8 cluster. The occupations of the lower and higher bands are 1.41 and 0.59, respectively. Two Fermi surfaces formed by the lower and higher bands are shown in Fig. 5. For $PbMo_6S_8$, two sheets of Fermi surfaces can be found, but they are not always well separated. This has implications for superconducting order parameters, as we

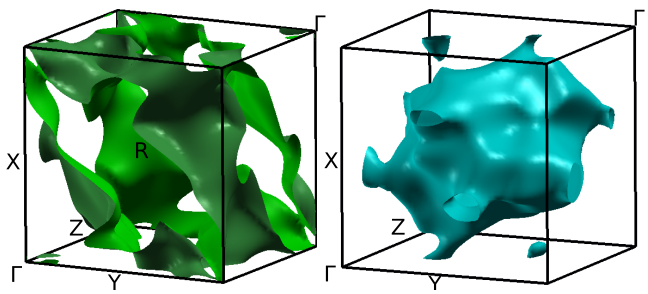

FIG. 5. Depiction of the Fermi surface of $PbMo_6S_8$ formed by the lower band (left panel) and the higher band (right panel) in the primitive cell of the reciprocal lattice. Both plots were generated by the XCRYSDEN package [35].

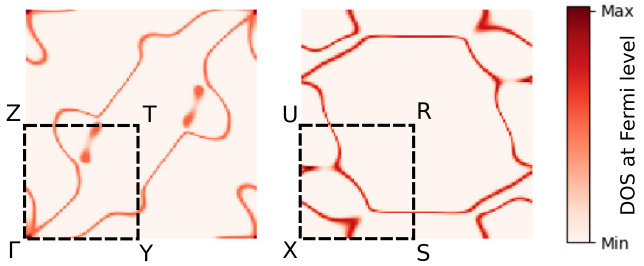

FIG. 6. Density of states at the Fermi level of $PbMo_6S_8$ in the XY planes through the Γ point (left panel) through the R point (right panel).

will discuss in Sec. V B. The Fermi surface associated with the lower band centered around Γ point is holelike and the Fermi surface associated with the higher band is electronlike. Two-dimensional cuts of the Fermi surfaces are shown in Fig. 6. On the XY plane through the R point (right panel), two separated Fermi surfaces are clear with the larger one as the electron pocket. It should be noted that two Fermi sheets touch each other at some places in the Brillouin zone. For example, at the Γ point, two bands can be found at Fermi level.

B. Electron-electron interactions

We performed constrained random phase approximation (cRPA) calculations of the effective interactions between electrons in the two frontier bands, following the approach developed by Aryasetiawan *et al.* [36]. The polarization matrix in reciprocal space was calculated in the random phase approximation as implemented in the BERKELEYGW package [37] with a $2 \times 2 \times 2$ k-point mesh, 100 unoccupied states, and kinetic energy cutoff of 5 Ry for the polarization matrix. The result is divided into contributions between states in the low-energy sector (P^{le}), which consists of two bands crossing the Fermi level, and processes involving transitions in at least one other band (P^r) as

$$P^{\text{tot}}_{\mathbf{GG}'}(\mathbf{q}) = P^{le}_{\mathbf{GG}'}(\mathbf{q}) + P^{r}_{\mathbf{GG}'}(\mathbf{q}). \tag{5}$$

A dielectric matrix representing screening by the other degrees of freedom is constructed from P^r as

$$\epsilon_{\mathbf{GG}'}(\mathbf{q}) = \delta_{\mathbf{GG}'} - v_{\mathbf{GG}'}(\mathbf{q}) P^{r}_{\mathbf{GG}'}(\mathbf{q}), \tag{6}$$

and the partially screened interaction is defined as

$$W(\mathbf{r}, \mathbf{r}') = \frac{4\pi}{\Omega} \sum_{\mathbf{qGG}'} v_{\mathbf{GG}'}(\mathbf{q}) e^{i(\mathbf{q}+\mathbf{G})\cdot\mathbf{r}} \epsilon^{-1}_{\mathbf{GG}'}(\mathbf{q}) e^{i(\mathbf{q}+\mathbf{G}')\cdot\mathbf{r}'}, \tag{7}$$

where $v_{\mathbf{GG}'}(\mathbf{q})$ is the bare Coulomb interaction and Ω is the volume of the unit cell.

The effective on-molecule interactions, namely, the Hubbard U and Hund's exchange coupling J, are obtained by projecting W onto the two E_g orbitals of the isolated molecule:

$$U_{nm} = \iint d\mathbf{r}\, d\mathbf{r}' \phi^*_n(\mathbf{r}) \phi_n(\mathbf{r}) W(\mathbf{r}, \mathbf{r}') \phi^*_m(\mathbf{r}') \phi_m(\mathbf{r}'), \tag{8}$$

$$J_{nm} = \iint d\mathbf{r}\, d\mathbf{r}' \phi^*_n(\mathbf{r}) \phi_m(\mathbf{r}) W(\mathbf{r}, \mathbf{r}') \phi^*_n(\mathbf{r}') \phi_m(\mathbf{r}'). \tag{9}$$

TABLE III. The values of the bare and screened local interactions in eV.

U_{bare}	U_{cRPA}	U'_{bare}	U'_{cRPA}	J_{bare}	J_{cRPA}
5.36	0.28	5.07	0.18	0.139	0.044

The bare and screened local electron-electron interactions are listed in Table III. The bare interactions are larger than the charging energies reported in Sec. II because the isolated molecule calculations include relaxation of other electronic degrees of freedom (on-molecule screening). We find that the screening is almost complete; the screened interactions are factors of ∼20 less than the bare interactions, in contrast to other other molecular materials including κ-ET organic [38], alkali-doped C_{60} and aromatic compounds [39]. The strong reduction of the interaction can be understood in terms of the very large dielectric constant arising from the rest of the bands $\epsilon_{\text{cRPA}} = \lim_{\mathbf{G}+\mathbf{q}\to 0} 1.0/\epsilon^{\text{cRPA}\,-1}_{\mathbf{GG}}(\mathbf{q}) = 24.0$. We also observe that, in contrast to the simple perovskite transition metal oxides even the Hunds coupling is significantly renormalized, consistent with reported results for organic molecular materials [39].

Given the bandwidth $W \approx 0.7$ eV found in band structure calculations, the interaction strengths we find confirm that $PbMo_6S_8$ is far from the Mott transition regime and that local correlation effects may be neglected. We may simply consider the material to be metallic with essentially weak electronic correlations.

IV. PHONON BAND STRUCTURE AND ELECTRON-PHONON COUPLING

A. Phonon band structure

Starting from the fully relaxed electronic structures presented in the previous section, we used density functional perturbation theory (DFPT) [40] to calculate the phonon band structure and density of states shown in Fig. 7. The calculated phonon density of states agrees reasonably well with the density of states inferred from neutron scattering experiments [41]. Both calculation and experiment show a sharp peak at about 4 meV, and two gaps around 17 and 40 meV.

We have calculated the normal modes and find that the sharp peak in the phonon DOS at 4 meV arises from two modes with large Pb displacements (these modes also contribute to the very large dielectric constant), in agreement with the experimental observation that the peak is absent in Chevrel phase compounds without Pb ions [41,42]. Previous work had suggested that the minimum in the DOS at 17 meV marked the separation between internal (on-molecule) and external (intermolecular) vibrations [41,43]. We find two internal modes below 17 meV, which suggests hybridization between internal and external modes is present below 17 meV, similarly to the result found with Born–von Kármán lattice dynamics calculations with Lennard-Jones potentials [44].

B. Electron-phonon coupling

We have used DFPT to calculate the matrix elements $g^{\upsilon}_{ij}(\mathbf{k}, \mathbf{p})$ describing the scattering of an electron at momentum $\mathbf{p}$ in band j to momentum $\mathbf{k}$ in band i by emission or absorption of a phonon mode υ at momentum $k - p$. The calculations were performed on a $4 \times 4 \times 4$ grid in the Brillouin zone and then interpolated onto fine grids via electron and phonon Wannier functions following Refs. [45,46] as implemented in the EPW code [47]. The fine electron grid is $32 \times 32 \times 32$ and the fine phonon grid is $16 \times 16 \times 16$. Computationally, phonon coarse grid is the most expansive one to increase. When phonon coarse grid expands from 2^3 to 3^3 and 4^3, calculated total electron-phonon coupling λ_{tot} goes from 1.10 to 2.15 and 2.29. Convergence with respect

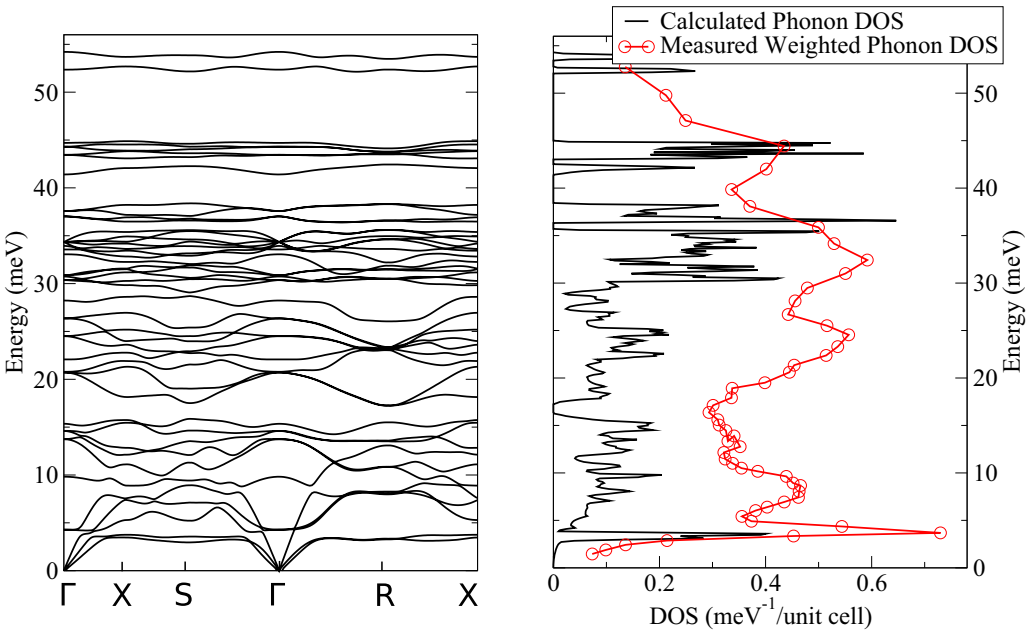

FIG. 7. Calculated phonon band structure (left panel), and calculated phonon density of states and measured neutron weighted phonon density of state (right panel), from Ref. [41].

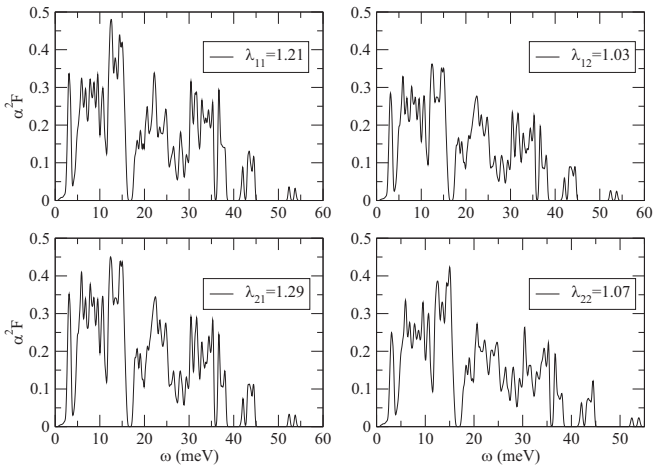

FIG. 8. Band-resolved electron-phonon interaction functions $\alpha^2 F$ from Eq. (10) and electron-phonon coupling constants from Eq. (11).

to electron and phonon fine grid is quite good. Difference of λ between grids of size 24^3, 12^3 and 32^3, 16^3 is smaller than 0.1.

From the matrix elements we calculate the band-resolved electron-phonon coupling function $\alpha^2 F$ as

$$\alpha^2 F_{ij}(\nu) = \frac{1}{N_i(0)} \sum_{\mathbf{k},\mathbf{p},\upsilon} \left|g^{\upsilon}_{ij}(\mathbf{k},\mathbf{p})\right|^2 \delta\left(\epsilon^i_{\mathbf{k}}\right)\delta\left(\epsilon^j_{\mathbf{k}-\mathbf{p}}\right)\delta\left(\nu-\omega^{\upsilon}_{\mathbf{p}}\right), \tag{10}$$

and the band-resolved total energy-phonon coupling constant as

$$\lambda_{ij} = 2\int_0^{\infty} \frac{\alpha^2 F_{ij}(\nu)}{\nu} d\nu. \tag{11}$$

Band-resolved electron-phonon spectral functions and coupling constants are shown in Fig. 8. The four αF_{ij} have similar structures, and give similar coupling constants. This is very different from the two-band superconductor MgB_2, for which intra-band coupling is much stronger than interband coupling [48]. We believe the difference arises because in MgB_2 the two bands arise from physically distinct π and σ orbitals whereas in the present case the two bands come from an on-molecule doublet.

The total coupling $\lambda_{\text{tot}} = \sum_{ij} \lambda_{ij} N_i(0)/[N_i(0) + N_j(0)] = 2.29$, is exceptionally large, larger than others found in other materials with strong electron-phonon couplings [49]. Density state at Fermi level derived from experimental specific heat $N_\gamma = 44.4/(\text{eV unit cell})$ (see Ref. [32] and references therein). Our band structure calculations combined with electron-phonon coupling gives $N_{BS} \times (1+\lambda) = 36.3/(\text{eV unit cell})$. The value is consistent with that estimated by Andersen and collaborators [18] but inconsistent with other published estimates [32].

From Fig. 8, one sees that the modes with largest coupling lie in the frequency range from 11 to 17 meV. At the Γ point, Pb-dominated modes form a low-lying transverse doublet around 5 meV and a longitudinal singlet around 10 meV. After these three modes, five modes can be observed below the gap at 17 meV. The atomic movement associated with these five phonon modes at the zone center (Γ point) and zone boundary (X point) are represented in Fig. 9. At the zone center, these five modes exhibit torsional character. External torsional modes have previously been suggested to be important for superconductivity based on a molecular crystal model [43]. At the zone boundary, these five modes show a character consistent with physics of dimerization, as a whole cluster rigidly moves towards its counterpart in the neighboring unit cell, albeit some mixing with other modes. Phonon modes with these characteristics are consistent with Peierls coupling [50]. At the zone center, phonons are limited to one unit cell, and rotations can impact the electron hopping between molecules by changing overlaps between molecular orbitals since molecular orbitals are generally not spherical (as shown in Fig. 2). At the zone boundary, phonons are extended to two neighboring unit cells, and dimerization can modify electron hopping by changing the distance between molecules. Based on the above observations, we conclude that in Chevrel phase compounds the most important contributions to the electron-phonon coupling are Peierls-type couplings from 11 to 17 meV.

To further understand the physics of those phonon modes, we calculated the variation of band structure due to the atomic displacement of the mode shown in Fig. 9(e). As we can see in Fig. 10, for the 11th phonon mode at Γ point, the bandwidth increases with atomic displacement; but the degeneracy from the Γ point to the R point is preserved. This degeneracy implies the phonon mode has no Jahn-Teller character; the increase of bandwidth illustrates that the main effect is an increase in the overlap of each Mo_6S_8 unit. This is the expected behavior from Peierls coupling: intermolecular hoppings vary with vibrations, but intramolecular states remain stationary. All information presented leads to the conclusion that strongest electron-phonon coupling in Chevrel phase compounds occurs via Peierls active modes.

V. CONSEQUENCES OF THE ELECTRON-PHONON INTERACTION

A. Normal-state self-energy

The normal-state self-energy due to the electron-phonon interaction was calculated in the Migdal approximation, using the one-loop diagram with noninteracting electron and phonon Green's functions and electron-phonon matrix elements obtained from our band structure. We separate the integral over the electron momentum into an energy and a Fermi surface integral and focusing on the band-diagonal terms in the self-energy we obtain

$$\Sigma_{ii}(z) = \int_{-\infty}^{\infty} d\epsilon \sum_{l\upsilon} \int_0^{\infty} d\nu\, \alpha^2 F_{il}(\nu) \times \left[\frac{1+n^{\upsilon}_{\nu}-f(\epsilon)}{z-(\nu+\epsilon)} - \frac{n^{\upsilon}_{\nu}+f(\epsilon)}{z-(-\nu+\epsilon)}\right]. \tag{12}$$

Here, i, l label the electronic bands, and υ labels phonon modes.

After analytically continuing the frequency argument z to the real axis, we compute the electron spectral function at

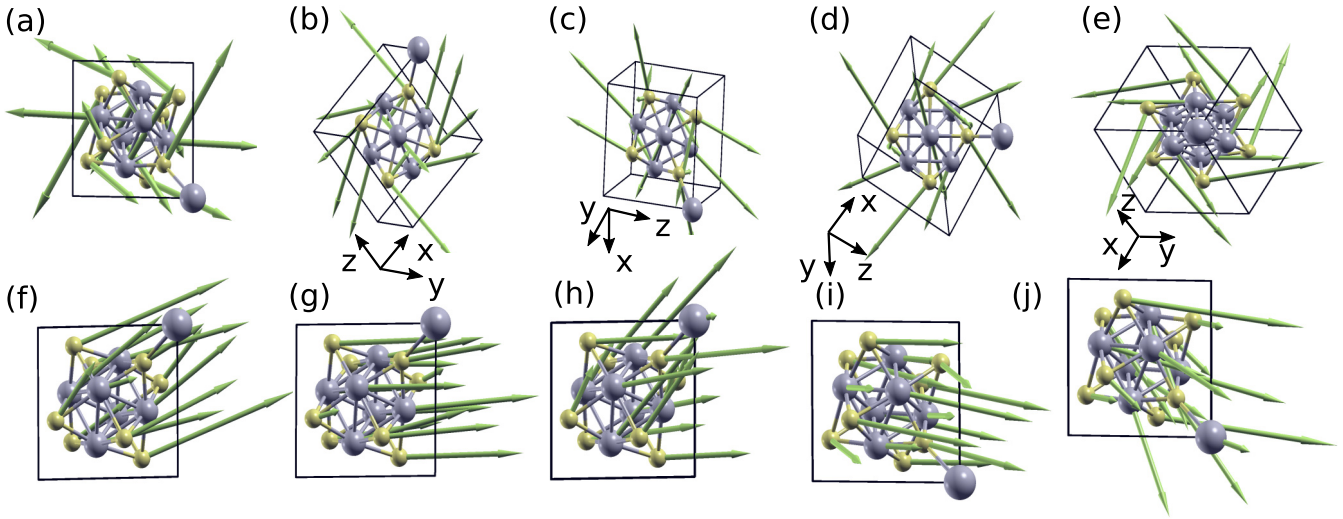

FIG. 9. The five Γ-point phonon modes of $PbMo_6S_8$ with energies in the range of 11.0 to 15.6 meV (a)–(e) and the X point (f)–(j) of Brillouin zone, Pb atom is at one vertex of the cubic unit cell. Green arrows represent real-space motion of atoms in the displayed phonon modes. Each subplot was generated by the XCRYSDEN package [35].

$T = 0$ as

$$A_i(\mathbf{k}, \omega) = \frac{1}{\pi}\mathrm{Im}\left(\frac{1}{\omega - \epsilon_i(\mathbf{k}) - \Sigma_{ii}(\omega - i\delta)}\right). \quad (13)$$

Results are shown in Fig. 11. We see that the electron-phonon interaction significantly modifies the dispersion only for energies within ∼20 meV of the Fermi surface, leading to velocity renormalization of a factor of 2–3 at these energies. The near correspondence of bare and renormalized velocities at higher energies shows that phonons at higher frequencies, including the internal Jahn-Teller modes at ∼30 meV, have a relatively small effect on the spectrum.

B. Superconductivity

With band-resolved electron-phonon spectral function defined in Eq. (10) and the self-energy evaluated in the Migdal approximation, we study strong coupling two-band superconductivity using the Eliashberg equations, following previous work on MgB_2 [51] and $Mg_{1-x}Al_xB_2$ [52]. The equations may be written on the imaginary axis as

$$\Delta_i(i\omega_n)Z_i(i\omega_n) = \pi T \sum_{m,j}[\lambda_{ij}(i\omega_m - i\omega_n) - \mu^*_{ij}] \times \frac{\Delta_j(i\omega_m)}{\sqrt{\omega_m^2 + \Delta_j^2(i\omega_m)}}, \quad (14)$$

$$Z_i(i\omega_n) = 1 + \frac{\pi T}{\omega_n}\sum_{m,j}\lambda_{ij}(i\omega_m - i\omega_n)\frac{\omega_m}{\sqrt{\omega_m^2 + \Delta_j^2(i\omega_m)}}, \quad (15)$$

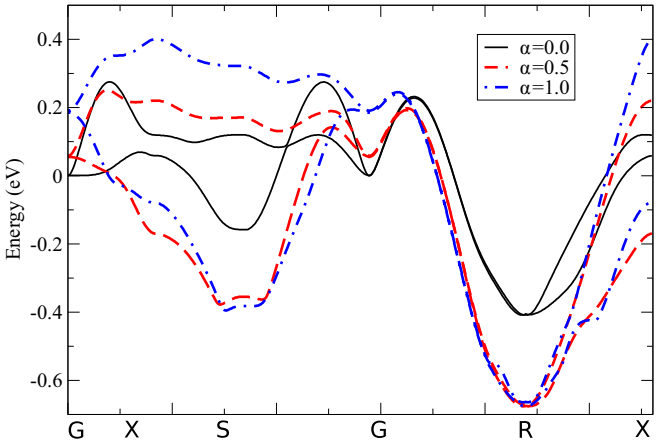

FIG. 10. Band structure of the 11th phonon mode at the Γ point, as shown in Fig. 9(e). Atomic poitions $\mathbf{X}$ for each calculation are determined by $\mathbf{X} = \mathbf{X_0} + \alpha\mathbf{u}$. $\mathbf{X}_0$ are the equilibrium atomic positions and $\mathbf{u}$ is the phonon mode displacement from the DFPT calculation.

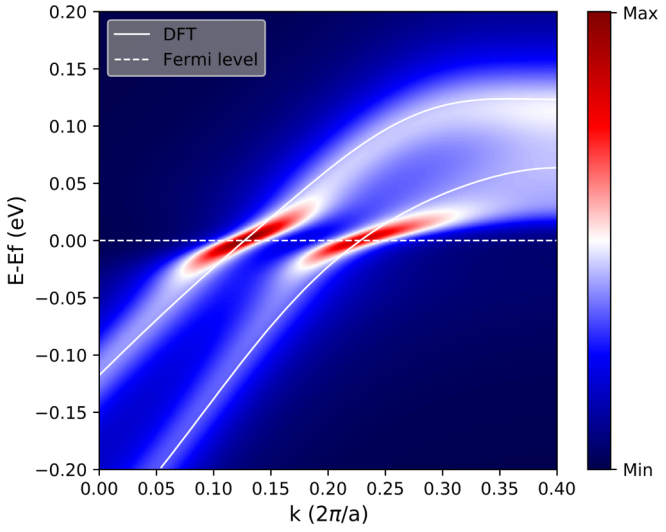

FIG. 11. False-color representation of electron spectral function with (shaded) and without (white line) electron-phonon interactions for near Fermi-surface momenta along the line from the R to the X point of the Brillouin zone.

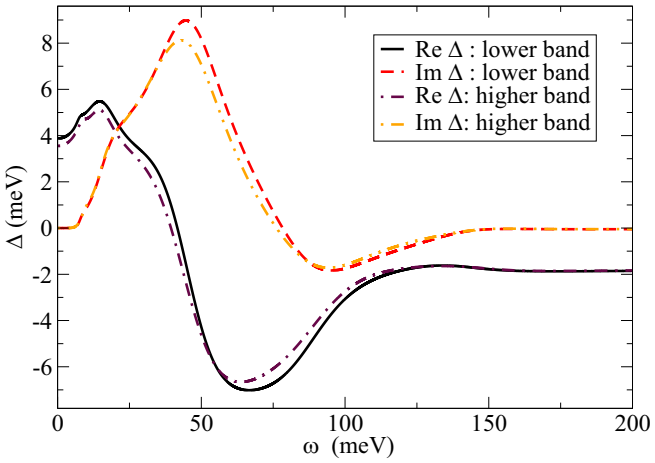

FIG. 12. Real and imaginary parts of the two gap functions as a function of energy as extracted from Padé approximants

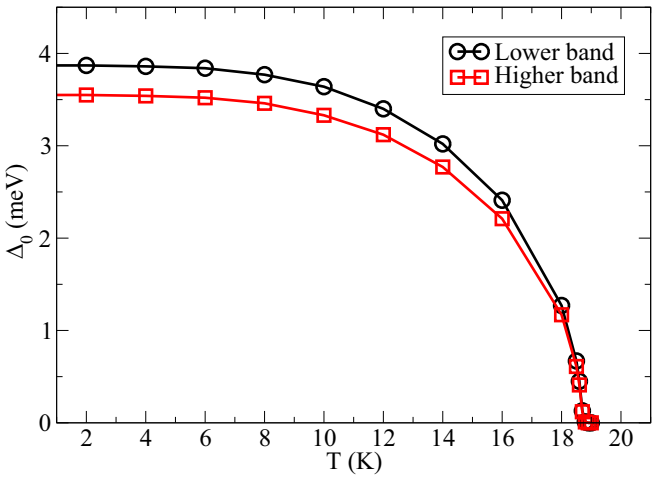

FIG. 13. Calculated superconducting gaps as function of temperature.

where $\Delta(i\omega_n)$ and $Z(i\omega_n)$ are superconducting gap and renormalization function; ω_n are discrete Matsubara frequencies at temperature T, and λ_{ij} is

$$\lambda_{ij}(i\omega_m - i\omega_n) = 2\int_0^\infty d\Omega \frac{\Omega\alpha^2 F_{ij}(\Omega)}{\Omega^2 + (\omega_n - \omega_m)^2}. \quad (16)$$

We estimated the Coulomb pseudopotential μ^*_{ij} within this theory via $\mu_{ij} = U\sqrt{N_i(0)N_j(0)}$. $U = 0.28$ eV used here is from a cRPA calculation, which gives $\mu_{ij} \approx 1.4$. The Coulomb pesudopotential reduced by retardation effects leads to [53]

$$\mu^*_{ij} = \frac{\mu_{ij}}{1 + \mu_{ij}\ln(E_{ele}/\omega_{ph})}. \quad (17)$$

The typical electron energy E_{ele} is approximated by the half-bandwidth of E_g bands: $W/2 \approx 0.35$ eV, and the relevant phonon frequency $\omega_{ph} \approx 12$ meV. (See the Bergmann-Rainer analysis below.) This method yields a Coulomb pseudopotential value of $\mu^*_{ij} \approx 0.24$.

Equations (14) and (15) were solved on the imaginary axis and the gap functions were analytically continued to the real axis via Padé approximants [54], as shown in Fig. 12. Superconducting gaps at the Fermi level as function of temperature are shown in Fig. 13. The T_c from our calculation is found out to be 18.8 K, which is larger than experimental value of 15 K by about 25%. In the framework of the two-band isotropic Eliashberg equations used in this work, two possible reasons for this are the inadequate treatment of the Coulomb interaction and the anisotropy of Fermi surfaces. As shown in recent work [55,56]. retardation effects are less effective in systems with strong coupling and narrow bands, which is the case for Chevrel phase compounds. In order to reproduce the experimental T_c with the calculated $\alpha^2 F_{ij}$, the Coulomb pseudopotential would need to be $\mu^*_{ij} \approx 0.9$. We found two isotropic superconducting gaps are $\Delta_1 = 3.93$ meV and $\Delta_2 = 3.59$ meV. Earlier tunneling spectroscopy had $\Delta = 2.4$ meV [57]; more recent experiment shows $\Delta_1 = 3.1$ meV and $\Delta_2 = 1.4$ meV [13]. The large gap from our calculation is reasonable, but the overestimation of the smaller gap is significant. This discrepancy may arise from an exaggeration of $\alpha^2 F$ from the DFPT calculations. Anisotropic calculations based on $\alpha^2 F$ from DFPT also overestimate T_c for multiband superconductors such as MgB_2 [58] and Ca-intercalated bilayer graphene [59].

Earlier interest in Chevrel phase superconductors stemmed from their very high upper critical field H_{c2}, which can be related to coherence length ξ_0 via $H_{c2} \propto 1/\xi_0^2$. Indeed, a very short coherence length (20 Å) has been reported based on magnetic measurements [60]. We can estimate coherence length within BCS theory via the superconducting gap and the Fermi velocity $\xi_0 = \frac{\hbar v_F}{\pi\Delta}$. We calculated the Fermi velocities for two bands based on the DFT band structure, and they are renormalized by the electron-phonon coupling as $v_F^{*i} = v_F^i/(1 + \sum_j \lambda_{ji})$. For the lower band $v_F^{*lb} = 1.09$ eV Å, $\xi_0^{*lb} = 173$ Å and for the higher band $v_F^{*hb} = 0.85$ eV Å, $\xi_0^{*hb} = 136$ Å. The calculated coherence length is about one order of magnitude larger than the those reported in experiment. This is not necessarily a contradiction with experiment, Chevrel phase superconductors are known to be found in the dirty limit [32,61], which implies measured coherence length is not an intrinsic property of pure crystal. Previously, the mean-free path l was estimated to be about 4 Å [62]. $\xi = \sqrt{l \times \xi^*}$ gives a coherence length about 25 Å, which is very close to reported experimental number 20 Å.

We now extend the calculations to the other Chevrel phase compounds, assuming the electron-phonon matrix elements $g^\nu_{ij}(\mathbf{k}, \mathbf{p})$ take on values of those of $PbMo_6S_8$, but using the material-specific electronic band structures. Five Chevrel phase compounds were studied, and they can be put into two categories: $M^{2+}Mo_6S_8$ and $M^{3+}Mo_6S_8$, corresponding to two distinct doping levels for the Mo_6X_8 units. It is established that Yb, Sn, and Pb belong to the first type and Y and La belong to the second type [61]. As shown in Table IV, the main difference between those two types is the occupation of lower band around Fermi level. For $M^{2+}Mo_6S_8$, occupation of the lower band is incomplete, so there still is large DOS at the Fermi level. For $M^{3+}Mo_6S_8$, the occupation of the lower band is close to full and the occupation of higher band is close to half. As a result, the lower band has very little contribution

TABLE IV. Experimental and calculated values of T_c, lattice constants, and the DOS for five Chevrel phase compounds. 1 and 2 label the lower and the higher band. Experimental data are from Refs. [61,63].

	Expt. T_c	Calc. T_c	Expt. a (Å)	Calc. a (Å)	$N_1(0)$	$N_2(0)$	$N(0)_{\text{tot}}$
$PbMo_6S_8$	15.0	18.8	6.55	6.55	5.66	5.10	10.78
$SnMo_6S_8$	13.0	17.2	6.52	6.52	6.12	4.30	10.42
$YbMo_6S_8$	8.8	16.2	6.50	6.49	3.52	6.74	10.26
$LaMo_6S_8$	7.1	11.0	6.51	6.52	0.94	6.60	7.54
YMo_6S_8	3.0	7.6	6.45	6.46	0.28	5.58	5.96

to the DOS at the Fermi level, and one finds effectively a single-band situation.

As shown in Table IV, our calculations reproduce the experimental trends across material family very well. The lattice constants are quantitatively reproduced as is the variation of the transition temperatures. The calculated transition temperatures correlate with the total density of state at the Fermi level. This correlation can also explain that $PbMo_6S_8$ has the highest T_c in Chevrel phase compounds since Pb^{2+} has largest ionic radius in the family of $M^{2+}Mo_6S_8$ compounds. Our calculation overestimates the absolute transition temperatures, with the overestimation being larger for the lower T_c values. A more detailed study of electron-phonon coupling across the entire material family is an important topic for future research.

To further address the question of which phonon modes are most important for superconductivity, we calculate the functional derivative of T_c with respect to $\alpha^2F_{ij}(\omega)$ following the scheme invented by Bergmann and Rainer [64], and later extended to two-band systems by Mitrović [65]. The interband spectral functions are not independent: $\alpha^2F_{ij}(\omega)/\alpha^2F_{ji}(\omega) = N_j(0)/N_i(0)$. Only their combination as expressed through the off-diagonal spectral function defined in Eq. (18) is meaningful [66]:

$$\alpha^2F_{od}(\omega) = \frac{N_i(0)\alpha^2F_{ij}(\omega) + N_j(0)\alpha^2F_{ji}(\omega)}{N_i(0) + N_j(0)}. \qquad (18)$$

Functional derivatives of relevant quantities are shown in Fig. 14. Since the three α^2F_{ij} are not very different, it is expected that their functional derivatives show similar features. At low frequencies, the functional derivatives increase linearly with frequency, and they reach a maximum at about 12 meV. This number is close to earlier suggestions based on the comparison of low-frequency phonons in $PbMo_6S_8$ and $PbMo_6Se_8$ [41–43].

As shown in Sec. II, Jahn-Teller active intramolecular modes are found at much higher frequencies than 12 meV. The Bergmann-Rainer analysis shows their relevance to superconductivity is eclipsed by modes at lower frequencies. Combined with the fact that phonons from 11 to 17 meV have the most important effect on the normal-state spectrum, it is clear that phonon modes in this frequency range are the drivers of superconductivity in Chevrel phase compounds.

This finding is significant because intermolecular phonon modes are generally thought to not be relevant for superconductivity because low-frequency phonon modes are less pertinent for superconductivity than the high-frequency ones [67]. As mentioned in Sec. I, superconductivity in faced-centered-cubic X_3C_{60} is thought to mainly arise from intramolecular vibrational modes [2,3]. On the other hand, Peierls couplings are frequently discussed in the context of metal-insulator transitions in low-dimensional materials. In particular, it has been shown for one-dimensional organic conductors, the Peierls instability suppresses superconductivity at lower temperatures [68–70]. Our work shows that the Peierls coupling is important for superconductivity in three-dimensional (3D) crystals such as Chevrel phase compounds.

VI. CONCLUSION

We studied intramolecular and intermolecular interactions in Chevrel phase compounds, using $PbMo_6S_8$ as a model compound. Band structure calculations revealed two bands around the Fermi level which originate from two E_g molecular orbitals and are about 0.7 eV wide. Constrained random phase approximation calculations estimated an onsite Hubbard U value of $U = 0.28$ eV and a value of Hund's exchange $J = 0.04$ eV. Moreover, quantum chemistry calculations of isolated molecules were carried out to parametrize the Jahn-Teller effect in Mo_6X_8 molecules. The Jahn-Teller stability energy is $E_{\text{JT}} = 0.18$ meV, which is smaller than the band kinetic energy and intramolecular Coulomb interaction values, but larger than the Hund's exchange. This energetic ordering is consistent with a metallic ground state. If the band kinetic energy can be reduced via methods like chemical intercalation to the extent that materials are in the strongly correlated regime, the ground state could be a nonmagnetic insulator

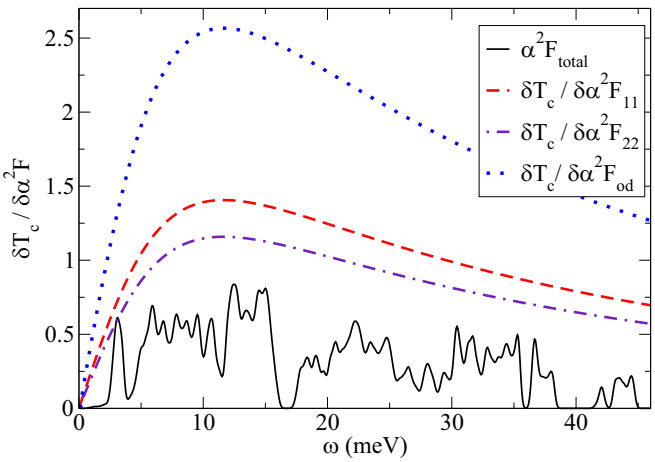

FIG. 14. Total electron-phonon spectral function, and functional derivative of T_c with respect to band-resolved spectral function. 1 and 2 label the lower and higher band.

because molecular Jahn-Teller effect suppresses Hund's coupling [71].

Density functional perturbation theory calculations with Wannier interpolations yield very strong electron-phonon coupling values, with $\lambda_{tot} = 2.3$. Visible modifications to the electronic bands near the Fermi level can be found in our calculated ARPES spectra. Band-resolved electron-phonon spectral functions reveal that the largest couplings are due to phonon modes in the frequency range from 11 to 17 meV. Phonon modes in this frequency range show the characteristics of Peierls-active modes.

Superconductivity was studied by two-band Eliashberg equations, with band-resolved electron-phonon spectral functions. Superconducting properties, T_c, and the larger superconducting gap are all in reasonable agreement with experiments. Our current theory overestimates the smaller superconducting gap. A Bergmann-Rainer analysis revealed that the most important phonon modes for superconductivity have frequencies around 12 meV, which is the spectral location of the largest electron-phonon coupling in $PbMo_6S_8$. To conclude, our work showcases the importance of intermolecular couplings for collective electronic behavior in molecular solids by illustrating a vital aspect that is overlooked in the standard molecular crystal model [72]. Internal Jahn-Teller active modes, which should be important for ground-state magnetic properties in the strongly correlated regime, are not responsible for superconductivity in Chevrel phase compounds.

ACKNOWLEDGMENTS

J.C. is supported by the NSF MRSEC program through Columbia in the Center for Precision Assembly of Superstratic and Superatomic Solids under Grant No. DMR-1420634. We used resources of the National Energy Research Scientific Computing Center, a DOE Office of Science User Facility supported by the Office of Science of the U.S. Department of Energy under Contract No. DE-AC02-05CH11231.

[1] X. Roy, C.-H. Lee, A. C. Crowther, C. L. Schenck, T. Besara, R. A. Lalancette, T. Siegrist, P. W. Stephens, L. E. Brus, P. Kim, M. L. Steigerwald, and C. Nuckolls, Science **341**, 157 (2013).
[2] C. M. Varma, J. Zaanen, and K. Raghavacharir, Science **254**, 989 (1991).
[3] O. Gunnarsson, Rev. Mod. Phys. **69**, 575 (1997).
[4] Y. Takabayashi, A. Y. Ganin, P. Jeglič, D. Arčon, T. Takano, Y. Iwasa, Y. Ohishi, M. Takata, N. Takeshita, K. Prassides, and M. J. Rosseinsky, Science **323**, 1585 (2009).
[5] W. Xie, H. Luo, B. F. Phelan, T. Klimczuk, F. A. Cevallos, and R. J. Cava, Proc. Natl. Acad. Sci. USA **112**, E7048 (2015).
[6] R. Chevrel, M. Sergent, and J. Prigent, J. Solid State Chem. **3**, 515 (1971).
[7] B. T. Matthias, M. Marezio, E. Corenzwit, A. S. Cooper, and H. E. Barz, Science **175**, 1465 (1972).
[8] R. Odermatt, O. Fischer, H. Jones, and G. Bongi, J. Phys. C: Solid State Phys. **7**, L13 (1974).
[9] Ø. Fischer, R. Odermatt, G. Bongi, H. Jones, R. Chevrel, and M. Sergent, Phys. Lett. A **45**, 87 (1973).
[10] Y. J. Uemura, L. P. Le, G. M. Luke, B. J. Sternlieb, W. D. Wu, J. H. Brewer, T. M. Riseman, C. L. Seaman, M. B. Maple, M. Ishikawa, D. G. Hinks, J. D. Jorgensen, G. Saito, and H. Yamochi, Phys. Rev. Lett. **66**, 2665 (1991).
[11] C. Dubois, A. P. Petrovic, G. Santi, C. Berthod, A. A. Manuel, M. Decroux, O. Fischer, M. Potel, and R. Chevrel, Phys. Rev. B **75**, 104501 (2007).
[12] F. J. Culetto and F. Pobell, Phys. Rev. Lett. **40**, 1104 (1978).
[13] A. P. Petrović, R. Lortz, G. Santi, C. Berthod, C. Dubois, M. Decroux, A. Demuer, A. B. Antunes, A. Paré, D. Salloum, P. Gougeon, M. Potel, and O. Fischer, Phys. Rev. Lett. **106**, 017003 (2011).
[14] D. Aurbach, Z. Lu, A. Schechter, Y. Gofer, H. Gizbar, R. Turgeman, Y. Cohen, M. Moshkovich, and E. Levi, Nature (London) **407**, 724 (2000).
[15] X. Zhong, K. Lee, B. Choi, D. Meggiolaro, F. Liu, C. Nuckolls, A. Pasupathy, F. De Angelis, P. Batail, X. Roy, and X. Zhu, Nano Lett. **18**, 1483 (2018).
[16] D. W. Bullett, Phys. Rev. Lett. **39**, 664 (1977).
[17] L. F. Mattheiss and C. Y. Fong, Phys. Rev. B **15**, 1760 (1977).
[18] O. K. Andersen, W. Klose, and H. Nohl, Phys. Rev. B **17**, 1209 (1978).
[19] F. Pobell, D. Rainer, and H. Wühl, Electron-phonon interaction in chevrel-phase compounds, in *Superconductivity in Ternary Compounds I: Structural, Electronic, and Lattice Properties*, edited by Ø. Fischer and M. B. Maple (Springer, Berlin, 1982), pp. 251–277.
[20] J. P. Perdew, J. A. Chevary, S. H. Vosko, K. A. Jackson, M. R. Pederson, D. J. Singh, and C. Fiolhais, Phys. Rev. B **46**, 6671 (1992).
[21] M. Valiev, E. Bylaska, N. Govind, K. Kowalski, T. Straatsma, H. V. Dam, D. Wang, J. Nieplocha, E. Apra, T. Windus, and W. de Jong, Comput. Phys. Commun. **181**, 1477 (2010).
[22] P. J. Hay and W. R. Wadt, J. Chem. Phys. **82**, 270 (1985).
[23] G. A. Petersson, A. Bennett, T. G. Tensfeldt, M. A. Al-Laham, W. A. Shirley, and J. Mantzaris, J. Chem. Phys. **89**, 2193 (1988).
[24] G. A. Petersson and M. A. Al-Laham, J. Chem. Phys. **94**, 6081 (1991).
[25] K. Momma and F. Izumi, J. Appl. Crystallogr. **44**, 1272 (2011).
[26] A. J. Millis, Phys. Rev. B **53**, 8434 (1996).
[27] C. A. Marianetti, D. Morgan, and G. Ceder, Phys. Rev. B **63**, 224304 (2001).
[28] J. P. Perdew, K. Burke, and M. Ernzerhof, Phys. Rev. Lett. **77**, 3865 (1996).
[29] P. Giannozzi, O. Andreussi, T. Brumme, O. Bunau, M. B. Nardelli, M. Calandra, R. Car, C. Cavazzoni, D. Ceresoli, M. Cococcioni, N. Colonna, I. Carnimeo, A. D. Corso, S. de Gironcoli, P. Delugas, R. A. D. Jr, A. Ferretti, A. Floris, G. Fratesi, G. Fugallo *et al.*, J. Phys.: Condens. Matter **29**, 465901 (2017).
[30] C. Hartwigsen, S. Goedecker, and J. Hutter, Phys. Rev. B **58**, 3641 (1998).
[31] M. Marezio, P. Dernier, J. Remeika, E. Corenzwit, and B. Matthias, Mater. Res. Bull. **8**, 657 (1973).

[32] Ø. Fischer, Appl. Phys. **16**, 1 (1978).
[33] A. A. Mostofi, J. R. Yates, G. Pizzi, Y.-S. Lee, I. Souza, D. Vanderbilt, and N. Marzari, Comput. Phys. Commun. **185**, 2309 (2014).
[34] N. Marzari and D. Vanderbilt, Phys. Rev. B **56**, 12847 (1997).
[35] A. Kokalj, Comput. Mater. Sci. **28**, 155 (2003).
[36] F. Aryasetiawan, K. Karlsson, O. Jepsen, and U. Schönberger, Phys. Rev. B **74**, 125106 (2006).
[37] J. Deslippe, G. Samsonidze, D. A. Strubbe, M. Jain, M. L. Cohen, and S. G. Louie, Comput. Phys. Commun. **183**, 1269 (2012).
[38] K. Nakamura, Y. Yoshimoto, T. Kosugi, R. Arita, and M. Imada, J. Phys. Soc. Jpn. **78**, 083710 (2009).
[39] Y. Nomura, K. Nakamura, and R. Arita, Phys. Rev. B **85**, 155452 (2012).
[40] S. Baroni, S. de Gironcoli, A. Dal Corso, and P. Giannozzi, Rev. Mod. Phys. **73**, 515 (2001).
[41] B. P. Schweiss, B. Renker, E. Schneider, and W. Reichardt, in *Superconductivity in d- and f-Band Metals, Second Rochester Conference*, edited by D. H. Douglass (Springer, Boston, MA, 1976), pp. 189–208.
[42] S. D. Bader, S. K. Sinha, and R. N. Shelton, in *Superconductivity in d- and f-Band Metals, Second Rochester Conference*, edited by D. H. Douglass (Springer, Boston, MA, 1976), pp. 209–221.
[43] S. D. Bader, G. S. Knapp, S. K. Sinha, P. Schweiss, and B. Renker, Phys. Rev. Lett. **37**, 344 (1976).
[44] S. D. Bader and S. K. Sinha, Phys. Rev. B **18**, 3082 (1978).
[45] F. Giustino, M. L. Cohen, and S. G. Louie, Phys. Rev. B **76**, 165108 (2007).
[46] F. Giustino, Rev. Mod. Phys. **89**, 015003 (2017).
[47] S. Poncé, E. Margine, C. Verdi, and F. Giustino, Comput. Phys. Commun. **209**, 116 (2016).
[48] A. A. Golubov, J. Kortus, O. V. Dolgov, O. Jepsen, Y. Kong, O. K. Andersen, B. J. Gibson, K. Ahn, and R. K. Kremer, J. Phys.: Condens. Matter **14**, 1353 (2002).
[49] P. Allen, in *Handbook of Superconductivity*, edited by C. P. Poole, Jr. (Academic, San Diego, CA, 2000), pp. 478–489.
[50] G. Mahan, *Many-Particle Physics*, 3rd ed. (Springer, Berlin, 2000), Chap. 7, pp. 433–495.
[51] E. J. Nicol and J. P. Carbotte, Phys. Rev. B **71**, 054501 (2005).
[52] G. Ummarino, R. Gonnelli, S. Massidda, and A. Bianconi, Phys. C (Amsterdam) **407**, 121 (2004).
[53] P. Morel and P. W. Anderson, Phys. Rev. **125**, 1263 (1962).
[54] H. J. Vidberg and J. W. Serene, J. Low Temp. Phys. **29**, 179 (1977).
[55] J. Bauer, J. E. Han, and O. Gunnarsson, J. Phys.: Condens. Matter **24**, 492202 (2012).
[56] J. Bauer, J. E. Han, and O. Gunnarsson, Phys. Rev. B **87**, 054507 (2013).
[57] U. Poppe and H. Wühl, J. Low Temp. Phys. **43**, 371 (1981).
[58] E. R. Margine and F. Giustino, Phys. Rev. B **87**, 024505 (2013).
[59] E. R. Margine, H. Lambert, and F. Giustino, Sci. Rep. **6**, 21414 (2016).
[60] D. N. Zheng, H. D. Ramsbottom, and D. P. Hampshire, Phys. Rev. B **52**, 12931 (1995).
[61] O. Peña, Phys. C (Amsterdam) **514**, 95 (2015).
[62] Ø. Fischer, D. Decroux, R. Chevrel, and M. Sergent, in *Superconductivity in d- and f-Band Metals, Second Rochester Conference*, edited by D. H. Douglass (Springer, Boston, MA, 1976), pp. 175–187.
[63] D. Hampshire, *Handbook of Superconducting Materials*, Vol. 2 (CRC Press, Boca Raton, FL, 2002), Chap. Chevrel Phase.
[64] G. Bergmann and D. Rainer, Z. Phys. **263**, 59 (1973).
[65] B. Mitrović, Eur. Phys. J. B **38**, 451 (2004).
[66] O. V. Dolgov and A. A. Golubov, Phys. Rev. B **77**, 214526 (2008).
[67] P. B. Allen and R. C. Dynes, Phys. Rev. B **12**, 905 (1975).
[68] L. Coleman, M. Cohen, D. Sandman, F. Yamagishi, A. Garito, and A. Heeger, Solid State Commun. **12**, 1125 (1973).
[69] J. Ferraris, D. O. Cowan, V. Walatka, and J. H. Perlstein, J. Am. Chem. Soc. **95**, 948 (1973).
[70] B. R. Patton and L. J. Sham, Phys. Rev. Lett. **31**, 631 (1973).
[71] M. Fabrizio and E. Tosatti, Phys. Rev. B **55**, 13465 (1997).
[72] T. Holstein, Ann. Phys. (NY) **8**, 325 (1959).